Hidden anomalies in topological t-PtBi$_{2-x}$ probed by second harmonic generation

Bryan L. Chavez [,1] Govinda Kharal,[1] Lingyi Xing,[2] Scott Crittenden [,1]
Thomas M. Crawford,[1] Yanwen Wu [,1] and Rongying Jin [1,2,*]

[1]*Department of Physics and Astronomy, SmartState Center for Experimental Nanoscale Physics,
University of South Carolina, Columbia, South Carolina 29208, USA*

[2]*Department of Physics and Astronomy, Louisiana State University, Baton Rouge, Louisiana 70803, USA*

The noncentrosymmetric Weyl semimetal PtBi$_{2-x}$ (t-PtBi$_{2-x}$) exhibits various interesting technologically important physical properties. We report the experimental investigation of PtBi$_{1.6}$ via second harmonic generation (SHG), single-crystal x-ray diffraction, magnetic susceptibility, and electrical resistivity measurements. While bulk structural, magnetic, and electrical properties show no phase transitions below room temperature, the temperature dependence of the SHG intensity reveals two anomalies: one at $T^* \sim 60$ K and another at $T_x \sim 200$ K. Quantitative analysis indicates that the SHG signal results from both the buckled Bi1 surface termination with the $3m$ symmetry and flat Bi2 surface termination with the m symmetry. However, the anomalies are mainly driven by Bi1 on the surface: (1) T^* marks the onset of surface states which is also manifested in the c-axis resistivity drop and (2) T_x corresponds to the lowest thermal contraction of the structure and enhanced magnetic susceptibility. This study demonstrates that SHG is a powerful technique for probing surface properties even for noncentrosymmetric materials.

I. INTRODUCTION

The most striking characteristic of topological materials is that they possess surface or edge states protected by the nontrivial topology of the bulk. For example, in Weyl semimetals, the surface is expected to form Fermi arcs with each arc connecting two Weyl nodes with opposite chirality [1–3]. Weyl electrons residing in Fermi arcs are considered a special type of two-dimensional (2D) electron gas with spin normal to the momentum in the reciprocal space [1,4]. In such semimetals, it is necessary to break either time-reversal or inversion symmetry [5,6]. Trigonal PtBi$_2$ (t-PtBi$_2$) has a noncentrosymmetric symmetry ($P31m$) with triply degenerate nontrivial bands near the Fermi level [7,8]. These nearly compensated electron and hole bands [7,8] make it an excellent Weyl semimetal. While angle-resolved photoemission spectroscopy (ARPES) has detected surface states with spin polarization, the experiments were performed at fixed temperatures of 40 K [9] and 15 K [10]. Additional surface electronic properties were investigated by scanning tunneling microscopy (STM) at 30 mK and 5 K, revealing two different terminations (Bi1 and Bi2) [11,12] consistent with that seen by ARPES [10]. With investigations at a few scattered temperatures (30 mK, 5 K, 15 K, 40 K, etc.), it is difficult to correlate surface properties with those seen in bulk. For example, is the extreme magnetoresistance (MR) at low temperatures [7,8,13] related to surface/edge states? How are surface properties such as superconductivity [11,14] related to bulk? Does the surface have reconstruction compared to its bulk?

In this article, we report the investigation of second harmonic generation (SHG) of t-PtBi$_{2-x}$ ($x \sim 0.4$) over a wide temperature range (5 K to 350 K). SHG provides information about symmetries related to a material's structural, electronic, and magnetic properties. Specifically, SHG at normal incidence is sensitive to in-plane surface symmetries. We find that the SHG signal consists of two contributions which can be understood from a consideration of $3m$ (from the buckled Bi1 termination and bulk) and m (from the flat Bi2 termination) symmetries. The SHG intensity also has unusual temperature dependence, including an enhancement below $T_x \sim 200$ K and a decrease below $T^* \sim 60$ K. Through careful comparison with other measurements on bulk crystal structure, electrical resistivity, and magnetic susceptibility, we consider these SHG anomalies reflect surface property changes.

II. EXPERIMENTAL DETAILS

PtBi$_{2-x}$ single crystals were grown using the self-flux method [8]. Energy dispersive x-ray spectroscopy shows a Bi deficiency with $x \sim 0.4$ [8]. Magnetic susceptibility measurements were carried out using a magnetic property measurement system (MPMS, Quantum Design) with a magnetic field of 1 T and temperature between 2 and 350 K. Resistivity measurements were carried out using a physical property measurement system (PPMS DynaCool, Quantum Design) with the standard four-probe technique. The crystal structure was determined via single-crystal x-ray diffraction (XRD) refinement at temperatures between 100 (2) K and 298 (2) K in intervals of 10 K. Single-crystal x-ray diffraction was performed using a Bruker D8 QUEST diffractometer equipped with a PHOTON-II area detector and an incoatec
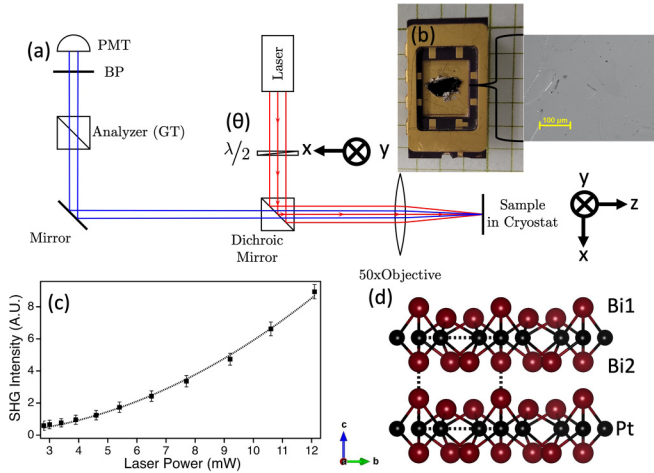
*rjin@mailbox.sc.edu

FIG. 1. (a) Second harmonic generation optical setup with a $50\times$ objective, an analyzer (Glan-Taylor polarizer), and a BP (bandpass filter). The sample is placed in the Montana Instruments Cryostation. (b) PtBi$_{2-x}$ sample on a chip carrier. A polarized microscope image is shown. (c) Laser power dependence of the SHG intensity. (d) Crystal structure of PtBi$_{2-x}$ with the indicated Pt, Bi1, and Bi2 layers.

microfocus source (Mo Kα radiation with the wavelength $\lambda = 0.71073$ Å). The sample was a lustrous plate of approximate dimensions $0.02\times0.08\times0.14$ mm^3 cleaved from a twinned aggregation. Upon reaching each temperature, the crystal was allowed to equilibrate for $\sim$5 minutes before data collection. At each temperature, three scans covering $12°$ were collected at three different angle settings ($0°$, $120°$, $240°$). A scan width of $0.6°$ was used, generating 20 frames at each angle setting. At each temperature, 135–150 reflections were collected from each scan, which were well separated in the reciprocal space. Unit cell parameters were then determined using the Bruker APEX3 autoindexing routine.

Figure 1(a) shows the setup for second harmonic generation measurements. The sample was attached to a chip carrier using silver paint, as shown in Fig. 1(b). Prior to the placement in an optical cryostat held at high vacuum (Montana Instruments Cryostation) the sample was cleaved to create a fresh surface. Polarized microscope images show a clean surface even after measurements [Fig. 1(b)]. A Ti:sapphire (Mira 900-HP) femtosecond pulsed laser was used with the wavelength set at 820 nm. SHG was performed at normal incidence, i.e., along the z direction [Fig. 1(a)]. A rotatable half-wave plate controlled the polarization of the beam with the polarization angle θ with respect to the x axis of the laboratory frame. A fixed dichroic mirror was used to direct the beam toward the sample and as a short-pass filter for the reflected SHG light. A fixed Glan-Taylor (GT) polarizer was used as an analyzer to resolve the polarization of the reflected light along the x and y directions (I_x and I_y). A prism and bandpass optical filter (FGB39, Thorlabs) were used before a photomultiplier tube (Hamamatsu, H9306-02) to remove the fundamental 820 nm light. The beam spot on the sample was $\sim$5 μm. SHG polarimetry was performed by rotating the input polarization while measuring the output signal intensity along either the x (I_x) or y polarization (I_y). Each polarization data point is an average of 300 measurements.

As demonstrated in Fig. 1(c), SHG intensity shows the typical quadratic behavior with laser power, validating the experimental setup [15,16]. Measurements were performed at a constant power of 7.8 mW, chosen to avoid surface damage. To be thorough, we measured the fundamental wavelength (ω) background independently for each data set and then subtracted it from the total to isolate the SHG signal (2ω). For cross-checking, SHG was performed on three crystal samples from two batches. For sample 1, measurements were repeated in 6 locations, while 4 locations were used for samples 2 and 3, respectively.

III. RESULTS AND DISCUSSION

Figure 1(d) shows the $P31m$ crystal structure of t-PtBi$_{2-x}$ as determined by single-crystal XRD at room temperature. The lattice parameters are $a = b = 6.5968$ Å and $c = 6.2143$ Å. The crystal symmetry and lattice parameters are consistent with that given in Refs. [7,17] for the stoichiometric case. Due to its noncentrosymmetry, the Bi1 layer is not equivalent to the Bi2 layer. The Bi2 atoms form a flat layer, whereas the Bi1 atoms are buckled. Both the Bi1 and Bi2 terminations can exist at the sample surface as confirmed by STM [11,12]. For our samples, STM also observed two terminations [18].

For SHG measurements, we start with $\theta = 0°$ and light along the z direction so that the electrical field is along the y direction, at which the sample rotation angle $\phi = 0°$. Figure 2(a) shows the polar plots of SHG intensities (I_x and I_y) at a temperature $T = 295$ K and $\phi \sim 0°$. While I_x (blue squares) reveals nearly perfect closed-loop 4-fold symmetry, I_y (red circles) shows a nonvanishing contribution in all directions in addition to the "four-lobe" pattern. For the bulk $P31m$ crystal structure, the $3m$ point group is expected and the nonzero SHG coefficients (d_{ij}) are $d_{15} = d_{24}$, $-d_{22} = d_{16} = d_{21}$, $d_{31} = d_{32}$, and d_{33}. Because the measurement is done in the normal incidence (light along the z direction), only the d_{22} term contributes to the measured SHG signal. This yields $I_x \propto d_{22}^2 \sin^2(2\theta)$ and $I_y \propto d_{22}^2 \cos^2(2\theta)$, producing no nonvanishing contributions. To figure out the origin of the nonvanishing component, we rotate the sample with an angle ϕ (light direction remains unchanged) and detect I_x and I_y at different ϕ values. The angle ϕ is with respect to one of the crystal's axes of high symmetry, i.e., where I_x is minimum and I_y is maximum in Fig. 2(a). Figure 2(b) shows the polar plots of I_x and I_y at the sample rotation angle $\phi \sim 30°$. From the sample rotation measurements, we observe nonvanishing contributions in both I_x and I_y. The amplitude of such nonvanishing contribution varies with ϕ. This implies that there is an additional contribution beside that from the $3m$ point group. While the Bi1 termination has the $3m$ symmetry [Fig. 2(c)], the Bi2 termination may contribute to SHG with the m symmetry [Fig. 2(d)].

The #SHAARP package [19] was used to assist fitting of the experimental data based on the combined $3m+m$ point groups. Since the fundamental beam is linearly polarized in the ab plane, $E_1 = E_0 \cos(\theta)$, $E_2 = E_0 \sin(\theta)$, and $E_3 = 0$. The theoretical expression, at $\phi = 0$, for I_x and I_y can thus
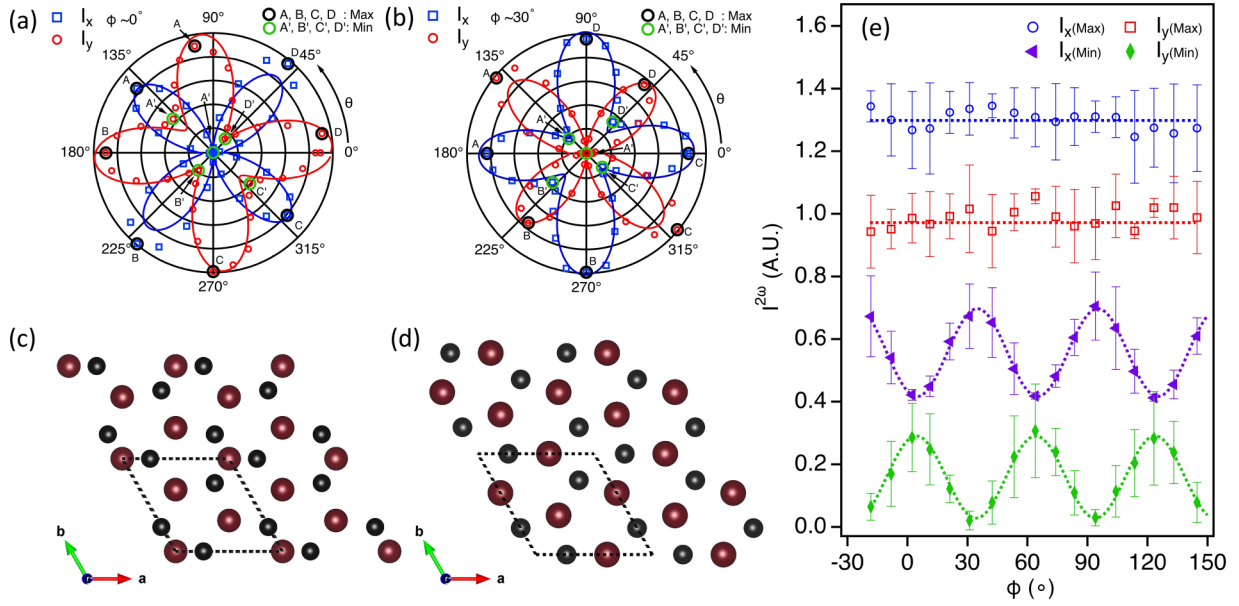
FIG. 2. (a) Polar plots of I_x (open squares) and I_y (open circles) obtained for $\phi \sim 0°$. (b) Polar plots of I_x and I_y with $\phi \sim 30°$ sample rotation. (c) Bi1 ($3m$) structure. (d) Bi2 (m) structure. (e) Sample rotation angle dependence of the SHG intensities of I_x(max), I_x(min), I_y(max), and I_y(min) which are obtained by averaging their corresponding maxima (A, B, C, and D) or minima (A', B', C', and D'). The dashed lines are guides for the eye.

be simplified to

$$I_x = I_x(m) + I_x(3m) \propto [d_{11}\cos^2(\theta) + d_{12}\sin^2(\theta)]^2 + d_{22}^2 \sin^2(2\theta), \tag{1}$$

$$I_y = I_y(m) + I_y(3m)$$
$$\propto d_{26}^2 \sin^2(2\theta) + d_{22}^2 \cos^2(2\theta). \tag{2}$$

Here, d_{11}, d_{12}, and d_{26} are from the m symmetry. The solid lines in Figs. 2(a) and 2(b) represent the fit of experimental data to Eqs. (1) and (2), respectively. Figure 2(e) shows the sample rotation angle ϕ dependence of the extreme intensity of I_x(max), I_x(min), I_y(max), and I_y(min) at $T = 295$ K. Here, I_x(max) $= \frac{1}{4}(I_x^A + I_x^B + I_x^C + I_x^D)$, I_x(min) $= \frac{1}{4}(I_x^{A'} + I_x^{B'} + I_x^{C'} + I_x^{D'})$, I_y(max) $= \frac{1}{4}(I_y^A + I_y^B + I_y^C + I_y^D)$, and I_y(min) $= \frac{1}{4}(I_y^{A'} + I_y^{B'} + I_y^{C'} + I_y^{D'})$. Here, superscripts A, B, C, and D denote the positions that SHG has the maximum intensity and A', B', C', and D' correspond to the minimum SHG intensity, which are indicated in Figs. 2(a) and 2(b). Following the dashed lines to guide the eye, one may see that I_x(min) and I_y(min) vary periodically with a period of $60°$, while I_x(max) and I_y(max) remain more or less constants. The latter is due to the fact that the major contribution is from the $3m$ symmetry, which is ideally a constant.

Upon changing the temperature, both I_x and I_y retain the same overall shape as those shown in Figs. 2(a) and 2(b). Figure 3(a) shows the temperature dependence of $\sqrt{I_x}$ (blue squares) and $\sqrt{I_y}$ (red circles). With decreasing temperature, both $\sqrt{I_x}$ and $\sqrt{I_y}$ initially increase with a larger slope below $T_x \approx 200$ K then decrease below $T^* \approx 60$ K. To further check this trend, we performed SHG measurements on different spots but collected the total unpolarized SHG signal. As shown in Fig. 3(b), the overall temperature dependence of

unpolarized SHG is similar to the polarized case [Fig. 3(a)]. Upon cooling from 350 K, the SHG response initially increases with a small slope (see the red dashed line that is a guide for the eye). Below T_x, the SHG intensity increases at a steeper rate until T^* then starts dropping below T^*.
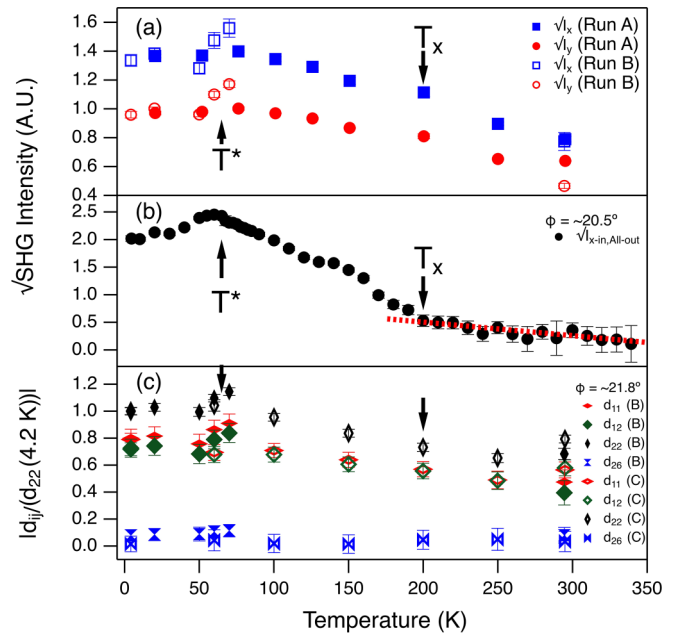

FIG. 3. (a) Temperature dependence of polarized $\sqrt{I_x}$ and $\sqrt{I_y}$ during two separate runs and spots (A, B). (b) Temperature dependence of unpolarized SHG intensity. The dashed line is the guide for the eye. (c) Temperature dependence of the extracted d_{ij} parameters for two different spots (B, C) obtained for $\phi \approx 20.5°$ and $\phi \approx 21.8°$, respectively.
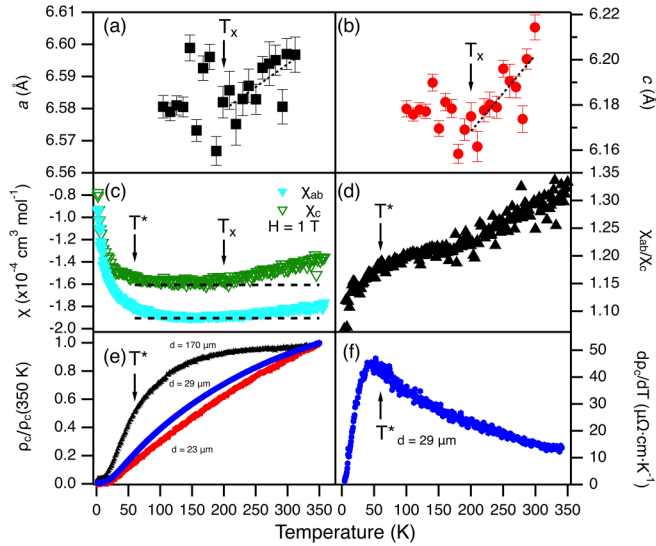
FIG. 4. (a), (b) Temperature dependence of the lattice parameters a (a) and c (b). Dotted lines are guides for the eye. (c) Temperature dependence of the magnetic susceptibilities χ_{ab} and χ_c; the horizontal dashed lines are for the minima. (d) χ_{ab}/χ_c versus temperature. (e) C-axis resistivity normalized as $\rho_c/\rho_c(350$ K$)$ obtained from samples with different thickness (170 μm, 29 μm, 23 μm). (f) $d\rho_c/dT$ versus temperature for sample with 29 μm thickness.

To identify the origin of the anomalous SHG at T^* and T_x, we fit I_x and I_y at all measured temperatures. Figure 3(c) shows the temperature dependence of d_{11}, d_{12}, d_{22}, and d_{26} at $\phi \approx 21.8°$. Note that (1) d_{22} reveals a similar trend as the unpolarized SHG, (2) d_{11} and d_{12} increase with decreasing temperature below ~250 K, and (3) d_{26} has little change in the entire temperature range. Based on this, the nonmonotonic temperature dependence of the SHG signal likely results from d_{22}, i.e., the $3m$ symmetry.

From the above analysis, we understand that the SHG signal is the combination of both the Bi1 ($3m$) and Bi2 (m) surface terminations and the bulk ($3m$). Given that the bulk also possesses a noncentrosymmetric symmetry belong to the $3m$ point group, an important question is whether the measured SHG is dominated by the surface or bulk contributions.

To answer this question, we carried out single-crystal XRD measurements between liquid nitrogen (the lowest temperature we can reach) and room temperature. Figures 4(a) and 4(b) show the temperature dependence of the lattice parameters a and c, respectively. Both a and c initially decrease with decreasing temperature due to thermal contraction. This trend seems reversed below $T_x \approx 200$ K; i.e., both a and c slightly increase with the further decrease of temperature. The crossover temperature T_x coincides with that seen in the SHG response. In normal circumstances, the negative thermal expansion below T_x would result in a reduced SHG response similar to that at higher temperatures. This implies that the bulk structure distortion at T_x [Figs. 4(a) and 4(b)] cannot be responsible for the enhanced SHG intensity below T_x. We thus consider the SHG anomalies to be due to the surface effect, i.e., driven by the Bi1 termination.

On the other hand, in view of the temperature dependence of the magnetic susceptibility for both the ab plane and c axis

shown in Fig. 4(c), we find that both χ_{ab} and χ_c are negative, reaching a minimum (marked by two horizontal dashed lines) around $T_x \approx 200$ K. Although they remain negative, the increase of χ_{ab} and χ_c below T_x should be attributed to the Curie-like temperature dependence of magnetic dipole interactions from free electrons [8]. This can qualitatively explain the increase in SHG intensity below T_x. However, this scenario would not explain the decrease of the SHG intensity below T^*, as the Curie susceptibility continuously increases with decreasing temperature. Figure 4(d) displays the temperature dependence of the ratio χ_{ab}/χ_c, which shows the deviation of χ_{ab}/χ_c below T^* from its high-temperature behavior. According to Eqs. (1) and (2), there should be no contribution from the c direction for normal incident. Therefore, it is unclear how magnetic anisotropy can influence the SHG response without further investigation.

Electrically, bulk PtBi$_2$ exhibits metallic behavior along the ab plane with the low residual resistivity [7,8,17]. However, when the sample thickness is reduced to 20 nm, nonmetallic behavior is observed, which is attributed to the disappearance of the buckled Bi1 termination because of the formation of $P\bar{3}$ structure [17]. If this were the case, it would be more impactful to the electrical conduction along the c axis. Figure 4(e) shows the temperature dependence of the c-axis resistivity ρ_c obtained from samples with different thicknesses. For easy comparison, the resistivity is normalized with respect to that at 350 K, i.e., $\rho_c/\rho_c(350$ K$)$. First, all samples show metallic behavior between 2 and 350 K. Upon decreasing the sample thickness, $\rho_c(T)$ changes from a convex shape to nearly linear behavior. The observed trend suggests that the system becomes more metallic as the sample gets thinner. According to Ref. [13], PtBi$_2$ with the $P\bar{3}$ symmetry is also metallic. In our case, there is no sign of a resistivity anomaly at either T_x or T^*.

With the lack of evidence for correlation between the SHG response and the bulk structural, magnetic, and electrical properties, we turn our attention to surface properties. As mentioned earlier, exciting phenomena are found from the buckled Bi1 surface, such as nontrivial band crossing [10] and a superconducting gap opening [11,14]. The measured surface superconducting gap value (~20 meV) is apparently too large for the low transition temperature of $T_c \approx 300$ mK to 3 K reported in Refs. [14,20]. On the other hand, this gap suggests surface superconductivity up to 100 K which is much closer to the characteristic temperature of $T^* \sim 60$ K [11].

For a centrosymmetric superconductor, the SHG intensity is expected to increase below T_c due to symmetry-breaking nonlinear supercurrents [21]. For a noncentrosymmetric superconductor, e.g., PbTaSe$_2$, giant second harmonic transport is observed below T_c leading to the reduced electric field $E^{2\omega}$ below T_c [22]. Reduced SHG intensity is thus expected in PtBi$_2$ if the surface Bi1 layer is superconducting [11,14]. Our data are consistent with this picture.

According to first-principles calculations, there are three topologically nontrivial gaps in monolayer PtBi$_2$, and each of these gaps hosts a robust one-dimensional electronic state on the sample boundary [12]. Such edge states have been observed via STM in both the Bi1 and Bi2 surfaces up to liquid nitrogen temperature. Our interest is how the exis-

tence of these edge states impacts the SHG response. Given the higher electrical conduction due to the edge states, one would expect reduced SHG intensity [23]. For $PtBi_{2-x}$, there is a sharper decrease of $\rho_c/\rho_c(350$ K$)$ below T^* than that at higher temperatures as shown in Fig. 4(f). This implies better electrical conduction below $\sim T^*$, which is also consistent with the sharp raise of the magnetic susceptibility [Fig. 4(c)] due to dominant free electron contribution. Whether T^* marks the onset of the surface superconductivity or edge state formation requires additional investigation, while the characteristic temperature (T^*) is comparable to estimated gaps [23].

Through the above discussion, we believe that the surface structures and corresponding properties of $PtBi_{2-x}$ deserve further investigation. With the incident electromagnetic wave (820 nm wavelength), how surface states due to the top monolayer respond to the optical excitation requires theoretical exploration. Given the subtle changes in the bulk structural, electrical, and magnetic properties, anomalies seen in the SHG response can only be due to a surface contribution which has a relationship with the bulk but is magnified depending on the nature of the surface. Our SHG study demonstrates the power of the technique for probing surface properties even in a noncentrosymmetric bulk system.

IV. SUMMARY

Trigonal $PtBi_{2-x}$ single crystals have been investigated by measuring the temperature dependence of SHG, XRD, magnetic susceptibility, and c-axis electrical resistivity. SHG intensity shows complex polarization dependence, which can be described by the combined $3m$ and m symmetries of the

Bi1 and Bi2 surface terminations and bulk. While there is no sign of any symmetry change between 4.2 K and 350 K, the SHG intensity varies nonmonotonically with temperature. Two SHG intensity anomalies were found: one at $T^* \approx 60$ K and another at $T_x \approx 200$ K. However, the temperature dependence measurements of the crystal structure including its lattice parameters, magnetic susceptibility anisotropy, and c-axis electrical resistivity with different thicknesses does not provide any notable fingerprint at either T^* or T_x, to suggest sizable bulk contributions to SHG anomalies. We thus attribute the observed SHG anomalies at T^* and T_x to surface effects as reflected in the d_{22} parameter. The possible existence of surface edge states and/or superconductivity due to the surface Bi1 layer may reduce the SHG intensity below T^*, which is consistent with the sharp decrease of ρ_c. While T_x corresponds to the minimum thermal contraction of the structure and magnetic susceptibility, the SHG enhancement below T_x reflects stronger surface response than the bulk. To confirm the role of the surface(s), further investigation is necessary, including surface structure determination of both the Bi1 and Bi2 terminations and the related surface edge states and/or superconducting transitions. From a future application point of view, understanding the effect of light on this catalytic compound with topological properties is extremely important as hot electrons (holes) may be generated at the surface with a long relaxation time [12,24,25].

[1] S.-Y. Xu, C. Liu, S. K. Kushwaha, R. Sankar, J. W. Krizan, I. Belopolski, M. Neupane, G. Bian, N. Alidoust, T.-R. Chang, H.-T. Jeng, C.-Y. Huang, W.-F. Tsai, H. Lin, P. P. Shibayev, F.-C. Chou, R. J. Cava, and M. Z. Hasan, Observation of Fermi arc surface states in a topological metal, Science **347**, 294 (2015).

[2] S.-M. Huang, S.-Y. Xu, I. Belopolski, C.-C. Lee, G. Chang, B. Wang, N. Alidoust, G. Bian, M. Neupane, C. Zhang, S. Jia, A. Bansil, H. Lin, and M. Z. Hasan, A Weyl fermion semimetal with surface Fermi arcs in the transition metal monopnictide TaAs class, Nat. Commun. **6**, 7373 (2015).

[3] B.-C. Lin, S. Wang, A.-Q. Wang, Y. Li, R.-R. Li, K. Xia, D. Yu, and Z.-M. Liao, Electric control of Fermi arc spin transport in individual topological semimetal nanowires, Phys. Rev. Lett. **124**, 116802 (2020).

[4] A. C. Potter, I. Kimchi, and A. Vishwanath, Quantum oscillations from surface Fermi arcs in Weyl and Dirac semimetals, Nat. Commun. **5**, 5161 (2014).

[5] I. Belopolski, P. Yu, D. S. Sanchez, Y. Ishida, T.-R. Chang, S. S. Zhang, S.-Y. Xu, H. Zheng, G. Chang, G. Bian, H.-T. Jeng, T. Kondo, H. Lin, Z. Liu, S. Shin, and M. Z. Hasan, Signatures of a time-reversal symmetric Weyl semimetal with only four Weyl points, Nat. Commun. **8**, 942 (2017).

[6] M. Z. Hasan, S.-Y. Xu, I. Belopolski, and S.-M. Huang, Discovery of Weyl fermion semimetals and topological Fermi arc states, Annu. Rev. Condens. Matter Phys. **8**, 289 (2017).

[7] W. Gao, X. Zhu, F. Zheng, M. Wu, J. Zhang, C. Xi, P. Zhang, Y. Zhang, N. Hao, W. Ning, and M. Tian, A possible candidate for triply degenerate point fermions in trigonal layered $PtBi_2$, Nat. Commun. **9**, 3249 (2018).

[8] L. Xing, R. Chapai, R. Nepal, and R. Jin, Topological behavior and Zeeman splitting in trigonal $PtBi_{2-x}$ single crystals, npj Quantum Mater. **5**, 10 (2020).

[9] Y. Feng, Q. Jiang, B. Feng, M. Yang, T. Xu, W. Liu, X. Yang, M. Arita, E. F. Schwier, K. Shimada, H. O. Jeschke, R. Thomale, Y. Shi, X. Wu, S. Xiao, S. Qiao, and S. He, Rashba-like spin splitting along three momentum directions in trigonal layered $PtBi_2$, Nat. Commun. **10**, 4765 (2019).

[10] W. Jiang, F. Zhu, P. Li, Y. Li, G. Wang, Q. Jing, W. Gao, M. Tian, J. Ma, W. Zhang, W. Luo, and D. Qian, Electronic structure of non-centrosymmetric $PtBi_2$ studied by angle-resolved photoemission spectroscopy, J. Appl. Phys. **128**, 135103 (2020).

[11] S. Schimmel, Y. Fasano, S. Hoffmann, J. Puig, G. Shipunov, D. Baumann, S. Aswartham, B. Büchner, and C. Hess,

High-T_c surface superconductivity in topological Weyl semimetal t-PtBi$_2$, arXiv:2302.08968.

[12] X.-A. Nie, S. Li, M. Yang, Z. Zhu, H.-K. Xu, X. Yang, F. Zheng, D. Guan, S. Wang, Y.-Y. Li, C. Liu, J. Li, P. Zhang, Y. Shi, H. Zheng, and J. Jia, Robust hot electron and multiple topological insulator states in PtBi$_2$, ACS Nano **14**, 2366 (2020).

[13] Q. Yao, Y. P. Du, X. J. Yang, Y. Zheng, D. F. Xu, X. H. Niu, X. P. Shen, H. F. Yang, P. Dudin, T. K. Kim, M. Hoesch, I. Vobornik, Z.-A. Xu, X. G. Wan, D. L. Feng, and D. W. Shen, Bulk and surface electronic structure of hexagonal structured PtBi$_2$ studied by angle-resolved photoemission spectroscopy, Phys. Rev. B **94**, 235140 (2016).

[14] A. Veyrat, V. Labracherie, D. L. Bashlakov, F. Caglieris, J. I. Facio, G. Shipunov, T. Charvin, R. Acharya, Y. Naidyuk, R. Giraud, J. van den Brink, B. Büchner, C. Hess, S. Aswartham, and J. Dufouleur, Berezinskii-Kosterlitz-Thouless transition in the type-I Weyl semimetal PtBi$_2$, Nano Lett. **23**, 1229 (2023).

[15] R. W. Boyd, *Nonlinear Optics*, 2nd ed. (Academic Press, San Diego, CA, 2003).

[16] M. Fiebig, V. V. Pavlov, and R. V. Pisarev, Second-harmonic generation as a tool for studying electronic and magnetic structures of crystals: Review, J. Opt. Soc. Am. B **22**, 96 (2005).

[17] A. Zhu, H. Wang, Z. Chen, Y. Han, M. Zhu, M. Han, X. Zhu, W. Gao, and M. Tian, Thickness-tuned magnetotransport properties of topological semimetal trigonal PtBi$_2$, Appl. Phys. Lett. **122**, 113101 (2023).

[18] Zheng Gai *et al.* (unpublished).

[19] R. Zu, B. Wang, J. He, J.-J. Wang, L. Weber, L.-Q. Chen, and V. Gopalan, Analytical and numerical modeling of optical second harmonic generation in anisotropic crystals using ♯SHAARP package, npj Comput. Mater. **8**, 246 (2022).

[20] G. Shipunov, I. Kovalchuk, B. R. Piening, V. Labracherie, A. Veyrat, D. Wolf, A. Lubk, S. Subakti, R. Giraud, J. Dufouleur, S. Shokri, F. Caglieris, C. Hess, D. V. Efremov, B. Büchner, and S. Aswartham, Polymorphic PtBi$_2$: Growth, structure, and superconducting properties, Phys. Rev. Mater. **4**, 124202 (2020).

[21] C. Vaswani, M. Mootz, C. Sundahl, D. H. Mudiyanselage, J. H. Kang, X. Yang, D. Cheng, C. Huang, R. H. J. Kim, Z. Liu, L. Luo, I. E. Perakis, C. B. Eom, and J. Wang, Terahertz second-harmonic generation from lightwave acceleration of symmetry-breaking nonlinear supercurrents, Phys. Rev. Lett. **124**, 207003 (2020).

[22] Y. M. Itahashi, T. Ideue, S. Hoshino, C. Goto, H. Namiki, T. Sasagawa, and Y. Iwasa, Giant second harmonic transport under time-reversal symmetry in a trigonal superconductor, Nat. Commun. **13**, 1659 (2022).

[23] R. Russell, N. Ratcliff, K. Ahadi, L. Dong, S. Stemmer, and J. W. Harter, Ferroelectric enhancement of superconductivity in compressively strained SrTiO$_3$ films, Phys. Rev. Mater. **3**, 091401(R) (2019).

[24] H. Chen, W. Zhu, D. Xiao, and Z. Zhang, CO oxidation facilitated by robust surface states on Au-covered topological insulators, Phys. Rev. Lett. **107**, 056804 (2011).

[25] C. R. Rajamathi, U. Gupta, N. Kumar, H. Yang, Y. Sun, V. Süß, C. Shekhar, M. Schmidt, H. Blumtritt, P. Werner, B. Yan, S. Parkin, C. Felser, and C. N. R. Rao, Weyl semimetals as hydrogen evolution catalysts, Adv. Mater. **29**, 1606202 (2017).